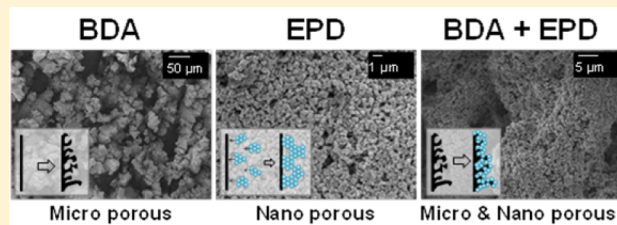


A Hybrid Method Employing Breakdown Anodization and Electrophoretic Deposition for Superhydrophilic Surfaces

Young Soo Joung and Cullen R. Buie*

Department of Mechanical Engineering, Massachusetts Institute of Technology, 77 Massachusetts Avenue, Cambridge, Massachusetts 02139, United States

ABSTRACT: A fabrication method is developed for superhydrophilic surfaces with high capillary pressure and fast spreading speed. The fabrication method consists of electrophoretic deposition (EPD) and breakdown anodization (BDA). Nanopores and micropores were produced on titanium plates by EPD and BDA, respectively. In EPD, TiO_2 nanoparticles were used to enhance the surface energy and create nanoporous structures, while BDA was employed to produce microporous structures. Capillary rise measurements (CRM) were utilized to characterize superhydrophilic surfaces in terms of capillary pressure and spreading speed. From CRM, it was revealed that microporous structures play a dominant role in determining transport properties, and nanoporous structures affect local wettability without significantly reducing spreading speed. By combining BDA and EPD into a hybrid method, dual-scale (nano and micro) porous structures were produced on titanium plates. The methods presented offer the potential to vary the transport characteristics of superhydrophilic surfaces by altering the nanoscale and microscale features independently. As an example, surfaces with unconventional capillary flows were produced by the hybrid method. This method provides additional opportunities to investigate wetting phenomena while offering a potentially low cost process for industrial applications.



INTRODUCTION

Superhydrophilic surfaces offer great opportunities to provide unique surface functions to practical applications such as antifogging glasses, heat sinks in pool boiling, heat pipes, evaporators, fuel spreaders, and microfluidic devices.^{1–5} Classically, superhydrophilic surfaces have been defined as surfaces that have contact angles of less than 5°.⁶ However, this criterion is not sufficient to precisely characterize superhydrophilicity, since superhydrophilic surfaces can show diverse behaviors in the above applications, even though all have similar static contact angles. Indeed, a definition of superhydrophilic surfaces has remained elusive.⁷ Therefore, appropriate parameters to characterize superhydrophilic surfaces and fabrication methods to control those parameters are necessary.

To realize superhydrophilicity, two key features, highly porous (rough) structures and high surface energy, are necessary.⁶ From Wenzel's equation,⁸ it is well-known that contact angles on a surface decrease with the increase of the surface roughness when the flat surface has a static contact angle less than 90°. Thus, it is necessary to achieve highly rough structures with nanomaterials or microfabrication techniques to produce superhydrophilic surfaces.^{4,9–13} In some cases, additional surface modifications with high surface energy materials are necessary.¹⁴ In most studies of superhydrophilic surfaces, the surfaces showed nearly zero contact angles, but they are rarely evaluated in terms of capillary pressure or spreading speed. Given the importance of transport properties, it is impossible to distinguish between superhydrophilic surfaces from contact angles alone. We believe that appropriate

characterization methods must be determined to precisely characterize superhydrophilicity.

Capillary pressure and spreading speed are well-known parameters for characterizing porous materials such as packed beads.¹⁵ Both parameters can be obtained from capillary rise measurements (CRM). Capillary pressure and spreading speed depend on the surface energy and bead size and are not generally proportional to each other. Thus, we consider them separately for evaluating superhydrophilic surfaces. In this study, we utilize CRM to characterize superhydrophilic surfaces. The surfaces can be considered as bundles of capillary tubes with various tube diameters.¹⁶

Recently, our group successfully produced superhydrophobic surfaces composed of SiO_2 nanoparticles using electrophoretic deposition (EPD).¹⁷ We employed low surface energy PDMS (polydimethylsiloxane) coated silicon dioxide (SiO_2) nanoparticles and controlled the suspension stability to produce highly rough surfaces. To produce superhydrophilic surfaces, we can use the same mechanism to achieve high porosity/roughness but with high surface energy particles. TiO_2 nanoparticles or nanotubes have been widely used to achieve high surface energy.^{9,13,18} However, it is challenging to simultaneously obtain high capillary pressure and fast spreading

Special Issue: Electrophoretic Deposition

Received: July 1, 2012

Revised: October 6, 2012

Published: October 15, 2012



speed due to high viscous resistance in small nanostructures, even though they show contact angles near zero.

In this work, we suggest a novel fabrication method to produce superhydrophilic surfaces with high capillary pressure and fast spreading speed. We show that the method can be utilized to control capillary pressure and spreading speed independently. EPD is utilized to obtain nanostructures composed of TiO₂ nanoparticles, while the breakdown anodization method (BDA) was employed to produce microporous structures. During anodization, the oxidation film thickness linearly increases with respect to electric potential.¹⁹ However, when the electric potential is higher than a critical value, the film thickness abruptly increases, resulting in a number of microscale irregularities. The critical electric potential is called the *breakdown point*. At electric potentials exceeding the breakdown point, microscale porous structures are created on the electrode. This phenomenon was reported a few decades ago but has not been exploited to produce superhydrophilic surfaces.^{20,21} Similar breakdown anodization methods have been used to produce nanoscale titanium structures such as nanotubes and nanowires on titanium substrates.^{22–28} These methods have typically used strong etchants in the electrolytes to locally etch the titanium substrate at the breakdown locations. The final nanostructures result from the balance between the etching rate and the oxidation rate. However, in our method, only mildly acidic electrolytes were used to make microscale titanium porous structures. This forces the need for higher electric potentials to initiate breakdown behavior. In addition, a balance between the dissolution rate of the oxide layer and the oxidation rate controls the resulting structures because weak electrolytes do not locally etch the titanium substrate.

EPD and BDA offer independent control of nanoscale and microscale features, respectively, resulting in a wide variety of superhydrophilic surfaces. We characterize these surfaces in terms of capillary pressure and spreading speed using CRM. The roles of nanopores (nanoscale spaces created by the nanoparticles and micropores (microscale spaces existing between microstructures) are investigated to understand the mechanisms governing capillary transport. Further, we demonstrate specially tailored superhydrophilic surfaces with spatially varying pore radii which result in unconventional capillary flows.

THEORY

Capillary flows can be characterized by Washburn's equation. Following this equation, the square of capillary height is linear with rising time. From this relation, two characteristic parameters, capillary pressure and spreading speed constant, can be semiempirically obtained. These parameters can be utilized to characterize superhydrophilic surfaces. EPD and BDA can be used to produce superhydrophilic surfaces with various capillary pressures and spreading speed constants. In EPD, suspension stability is important to control nanoscale structures.¹⁷ In BDA, microscale porous structures are created on anode electrodes when the anodization electric potential is higher than a critical value. The following sections outline the theoretical considerations necessary to fabricate and control transport in surfaces produced with BDA and EPD.

1. Capillary Flow. If the capillary forces exceed the gravitational force, the wetting line can rise. Washburn's equation has been widely used to predict the speed of capillary rise and can be expressed by¹⁶

$$\frac{dh}{dt} = \frac{r^2}{8\eta h} \left[\frac{2\gamma \cos \theta}{r} - \rho gh \right] \quad (1)$$

where h is the height of the wetting line; t is the time after contact with liquid; r is the pore radius; η , γ , and ρ are the dynamic viscosity, surface tension, and density of liquid, respectively; θ is the native contact angle of surface material; and g is the gravitational constant.

If the effect of gravity is negligible and the pore radius is constant, the relation between the capillary rise height and time can be expressed by

$$h^2 = \frac{r\gamma \cos \theta}{2\eta} t = \frac{1}{2} C_{\text{cap}} t \quad (2)$$

where C_{cap} is the spreading speed constant. From CRM, the change of capillary height with respect to time can be obtained and the spreading speed constant can be calculated by curve fitting.

Capillary pressure can be calculated from the maximum capillary height, since under this condition the capillary force balances the gravitational force, assuming liquid evaporation is negligible. Thus, the capillary pressure can be expressed by

$$P_{\text{cap}} = \frac{2\gamma \cos \theta}{r} = H_{\max} \rho g \quad (3)$$

where H_{\max} is the maximum capillary height. From eqs 2 and 3, we can semiempirically calculate the capillary pore size, r , and the contact angle, θ , as follows

$$r = \left(\frac{2\eta C_{\text{cap}}}{P_{\text{cap}}} \right)^{1/2} \quad \text{and} \quad \theta = \left(\frac{\eta C_{\text{cap}} P_{\text{cap}}}{2\gamma^2} \right)^{1/2} \quad (4)$$

If the pore radius is not constant but a function of h , we can obtain various profiles of contact line propagation.

2. Electrophoretic Deposition. The electrophoretic mobility, μ , is linearly proportional to the zeta-potential, ζ , and the permittivity, ϵ , of the medium, and is inversely proportional to the viscosity of the medium, η , as expressed by²⁹

$$\mu = \frac{2\epsilon\zeta}{3\eta} \quad (5)$$

assuming spherical particles where the Debye length is small relative to the particle radius.

During EPD, the deposition rate, \dot{M} , is a function of the mobility, the particle concentration, C , and the electric field, E , subjected to the electrodes as follows

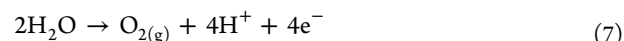
$$\dot{M} = \mu \cdot C \cdot E \quad (6)$$

Thus, if the concentration and the electric field are fixed during the EPD process, the deposited mass can be altered by the deposition time.

3. Anodization Process. On the Pourbaix diagram of titanium–water systems,³⁰ cathode and anode potentials during breakdown anodization correspond to the immunity and passivity regimes, respectively. The chemical reaction processes on the anode and the cathode electrodes we consider are as follows:

<Anode>

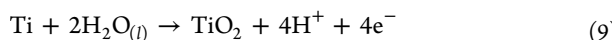
Electrolysis:



Corrosion:



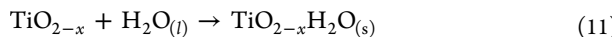
Oxidation:



Oxidation:



Dissolution:



Dissolution:



< Cathode >

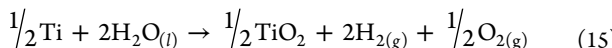
Electrolysis:



Electrodeposition:



Electrolysis (7) and dissolution (11) are continuously observed during the anodization process. Corrosion and electrodeposition can be expected in the initial stage of the anodization process, but these processes quickly terminate because the oxide layer prevents further corrosion (8). At steady state, the electrolysis, oxidation, and dissolution processes remain. Therefore, the overall anodization reaction in aqueous electrolytes can be expressed as



considering both oxidation and electrolysis processes. Given this, two dissolution processes (11) and (12) can be taken into account on the anode electrode. Through the dissolution process (11), hydrated titanium oxide sedimentations are observed in electrolytes after the anodization process. Then, the increase of pH of the electrolyte during the anodization process can be explained by the dissolution process (12).

4. Breakdown Potential. The general breakdown phenomenon was theoretically investigated by Sato.³¹ He suggested that the surface pressure, P , of the electrode during the anodization process can be estimated by the summation of the electrostriction effect and the interfacial tension effect as follows:

$$P = P_o + \frac{\varepsilon(\varepsilon - 1)E^2}{8\pi} - \frac{\gamma_e}{h_a} \quad (16)$$

with the ambient pressure P_o , the electric field E , the surface tension of the anodic oxide film γ_e , and the anodic oxide film thickness h_a . When the surface pressure is higher than the critical compressive stress of the film σ_o , the breakdown process takes place during anodization. If surface tension effects are considered, the electrochemical properties of electrolyte and electrode must be taken into account to estimate the breakdown conditions because ion adsorption under the film surface influences surface tension. The breakdown electric field, E_o , on the oxide layer can be expressed as a function of the electric potential, $E_c = (\phi - \phi_f)/h_a$, where ϕ is the electrode potential and ϕ_f is the equilibrium potential at the interface

between the oxide layer and the electrolyte. Finally, when breakdown is initiated, the electrode potential, ϕ^* , can be expressed by³¹

$$\frac{d\phi^*}{d\ln a} = -\frac{8\pi k_B T \rho_a}{8\pi\sigma_o - \varepsilon(\varepsilon + 1)E_c} \quad (17)$$

where a is the activity of anion in the electrolyte and ρ_a is the adsorption density of anions. From eq 17, we expect that high temperature electrolytes and high anion adsorption under the film surface lower the critical potential.

5. Effect of Electrolyte Temperature on Oxide Films.

For identical electrolytes, the maximum oxide film thickness is governed mainly by the electrolyte temperature and electric potential during the anodization process. The dissolution process (11) expresses the dissolution reaction governing the total oxide film thickness. This reaction is the hydration of the titanium oxide, which is soluble in acidic solutions. Electrolyte temperature affects the rate of this hydration step. In other studies, it has been generally accepted that, with increasing electrolyte temperature, the hydration rate also increases.^{32,33} This behavior can be verified by investigating the oxide film thickness with respect to electrolyte temperature. The oxide film thickness can be measured using the capacitance, C_f , of the oxide layer. The inverse capacitance, C_f^{-1} , is proportional to the oxide film thickness.³⁴ An empirical relationship between the capacitance and electrolyte temperature was suggested by Bockris et al. as follows:³⁵

$$\left. \frac{d\ln(C_f^{-1})}{dt} \right|_{C_f^{-1}} = -\frac{\Delta H}{RT} \quad (18)$$

where the activation energy is $\Delta H \sim 110.5$ kJ/mol and R is the universal gas constant. From eq 18, we find that the rate at which the oxide film thickness increases is inversely proportional to the electrolyte temperature.

EXPERIMENTAL METHODS

EPD and BDA were used to produce superhydrophilic surfaces. By combining both methods, we were able to make three different types of superhydrophilic surfaces: EPD only, BDA only, and a hybrid BDA/EPD method. Schematic illustrations of BDA and EPD are shown in Figure 1a and b, respectively. For EPD, TiO_2 nanoparticles (Sigma-Aldrich, titanium oxide, anatase, nanopowder, <25 nm particle size, ≥99.7% purity) were used. Acetic acid was used as solvent to prepare 1 g/L concentrations of TiO_2 suspensions. Titanium plates (Ultra-

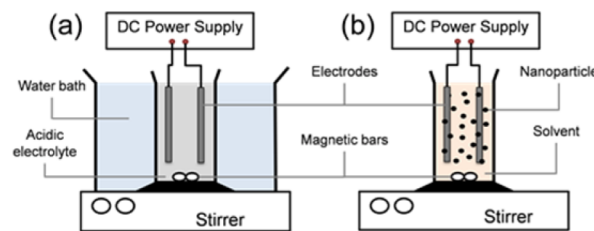


Figure 1. Schematic illustration of the experimental setups for breakdown anodization (BDA) (a) and electrophoretic deposition (EPD) (b). The water temperature is controlled to maintain constant electrolyte conditions during BDA. TiO_2 nanoparticles are dispersed in acetic acid solvents with 1 wt % concentration for EPD. The solvents of both methods are stirred with magnetic bars.

Corrosion-Resistant Titanium grade 2, 0.020" thick) were used as anode and cathode electrodes. An electric potential of 30 V was subjected to the electrodes (the gap distance between the electrodes was 10 mm) for 30–120 s to deposit thin films on the substrate. During BDA, the DI water was adjusted to pH 3 by adding acid (nitric acid, 70% ACS reagent, Sigma-Aldrich). Two titanium plates (same material used for EPD) were used as cathode and anode electrodes (the gap distance between electrodes was 10 mm), and electric potentials were supplied in the range 30–120 V for 30 min.

During BDA, the electrolyte temperatures were maintained at 10–75 °C because breakdown initiation is affected by electrolyte temperature, as shown in eq 17. Furthermore, it has been reported that electrolyte temperature affects the resulting electrode morphology.^{20,36} Therefore, the temperatures were adjusted using a circulating bath (polystate, Cole-Parmer) in order to investigate the effect of electrolyte temperature on wetting properties. Throughout BDA experiments, the electrolyte was rigorously stirred with a magnetic bar.

To produce nano- and microscale hierarchical structures on the titanium substrates, we used a hybrid BDA/EPD method. In this method, BDA was conducted first and then the anodized electrode was reused as the substrate for EPD. The EPD process in the hybrid method was conducted with the same operating conditions as the surfaces modified solely by EPD.

CRMs were performed to evaluate the capillary pressure and the spreading speed of the superhydrophilic surfaces. Figure 2

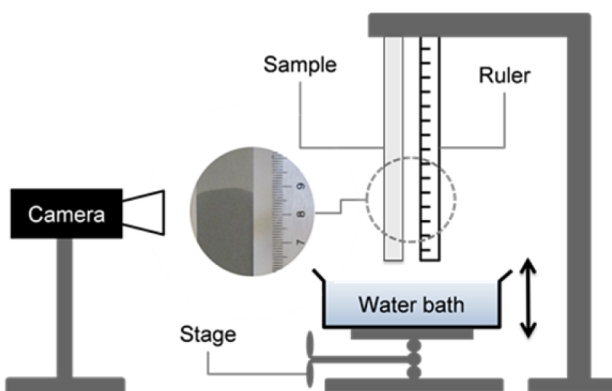


Figure 2. Schematic illustration of the capillary rise measurement (CRM) system. Capillary height is recorded by a digital camera and estimated with customized image processing software (Labview). Evaporation from the sample surface is prevented by encapsulating the sample in a glass column.

shows a schematic illustration of the CRM setup. During CRM, the sample is enclosed in a glass column to prevent evaporation from the surface during the test. The sample is fixed vertically, and the height of the water bath is gradually increased to make contact between the bottom of the sample and the water surface. Capillary rise through the substrate is recorded with a digital camera (Canon, PowerShot S90). A ruler fixed adjacent to the substrate is used to estimate the capillary rise height with respect to time.

Morphologies of the deposited films were characterized with a scanning electron microscope (SEM, JEOL 6320FV Field-Emission High-resolution SEM). Static contact angles (CA) were calculated using the tangential curve-fitting method. A goniometer (Kyowa, DM-CE1) was used to dispense and image a 3 μL drop of DI water on each sample. X-ray diffraction

(XRD) data were collected from the PANalytical X'Pert Pro Multipurpose Diffractometer with Cu anode material at 45 kW and 40 mA to investigate the material composition and atomic structure of the resulting surfaces. The step size and the scan step time are $2\theta = 0.017$ and 42.55 s, respectively.

RESULTS AND DISCUSSION

Figure 3 shows SEM images of the fabricated surface structures under different magnifications. Highly irregular and entangled

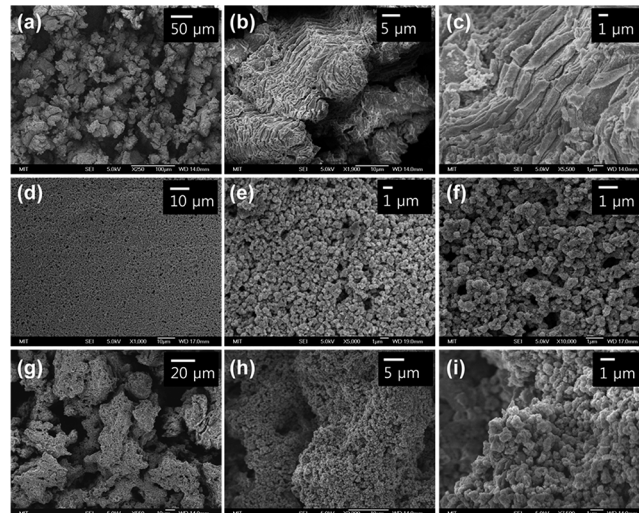


Figure 3. SEM images of superhydrophilic surfaces fabricated by breakdown anodization (BDA) (a–c), electrophoretic deposition (EPD) (d–f), and the hybrid BDA/EPD method (g–i). BDA was conducted at the electric potential 90 V for 30 min with an acidic electrolyte (pH 3) at 10 °C. EPD was conducted with the electric potential 30 V for 90 s with 1 wt % TiO₂ in an acetic acid solvent at ambient temperature. The surface produced by BDA consists of several entangled microporous structures, while the surface deposited with TiO₂ nanoparticles by EPD shows uniformly distributed nanoporous structures. The hybrid BDA/EPD method yields hierarchical micro- and nanoporous structures.

microstructures appear on the titanium electrode after BDA in Figure 3a–c. In the samples prepared by EPD with a 90 s deposition time, well ordered TiO₂ nanoparticles were observed, as shown in Figure 3d–f. Hierarchical structures, as shown in Figure 3g–i, were observed in the case of the hybrid BDA/EPD method. Here, the microstructures were highly curved and entangled, while TiO₂ nanoparticles were well dispersed on the surface. This suggests that the anodized surfaces do not completely lose their electrical conductivity.

Static contact angles were measured on each of the modified substrates. Each surface exhibited contact angles near 0°. Therefore, following the classical definition of superhydrophilic surfaces,⁶ the three fabrication processes resulted in superhydrophilicity. However, the time required to achieve zero contact angle differed among the samples. This reveals that the samples in fact have differing wettabilities, which is not evident from static contact angle measurements.

To further evaluate the superhydrophilic surfaces, spreading speed and capillary pressure were measured with CRM, as shown in Figure 2. As can be expected from eq 2, the square of capillary rise height is linearly proportional to time (Figure 4a). The slope of each linear fit line represents the spreading constant, $1/2 C_{cap}$. Capillary pressures were calculated from eq 3

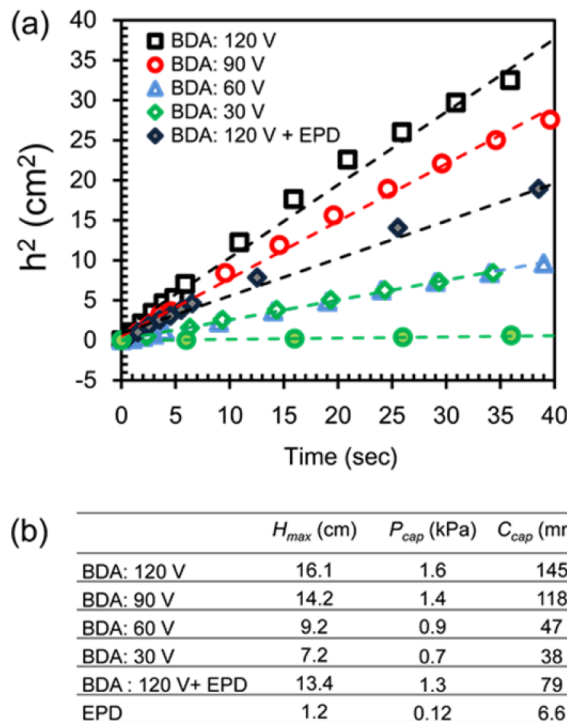


Figure 4. The square of experimentally derived capillary rise height is linearly proportional to time, as predicted by Washburn's equation (a). The samples produced by BDA and EPD show different capillary pressures and spreading speeds (b). The sample produced by the hybrid BDA/EPD method shows slightly lower spreading speed than the sample produced by BDA under the same conditions. In BDA, electrolyte temperatures were maintained at 10 °C and electric potentials were supplied for 30 min. EPD was conducted at the electric potential 30 V for 90 s. The spreading speed constant, C_{cap} , of the surface can be obtained from the slope of each curve, as shown in eq 2. The capillary pressure is calculated from eq 3 using the maximum rise height.

using the maximum capillary rise height of each surface. The surfaces produced by BDA show higher capillary pressure and spreading speed constant than the surfaces produced by EPD. This is attributed to the pore sizes of each surface. The BDA surfaces have microscale pores, as shown in Figure 3a–c, while the EPD surfaces are composed of nanoscale pores, as shown in Figure 3d–f. From eq 2, the spreading speed constant is linearly proportional to the effective pore radius. Therefore, it is reasonable to expect the BDA surfaces to show higher spreading speed constants than the EPD surfaces. However, unlike the capillary spreading constant, capillary pressure is inversely proportional to the pore radius. Viscous drag through smaller pores reduces capillary speed at low heights. For time scales on the order of days, the capillary rise height of the EPD surfaces can be considered as quasi-static. Therefore, the EPD surfaces have lower effective capillary pressures than the BDA surfaces even though the pore size is significantly smaller. Interestingly, the surfaces produced by the hybrid BDA/EPD method maintained both high capillary pressure and spreading speed constant. From this result, we conclude that the overall transport characteristics are governed by microscale structures and only locally influenced by the nanoscale structures.

Different electric potentials and electrolyte temperatures during BDA were investigated to control wettability and capillary transport properties. Capillary pressure and spreading speed constant with respect to electric potentials and

electrolyte temperatures are shown in Figure 5a and b. Interestingly, for a given temperature, the electric potential to

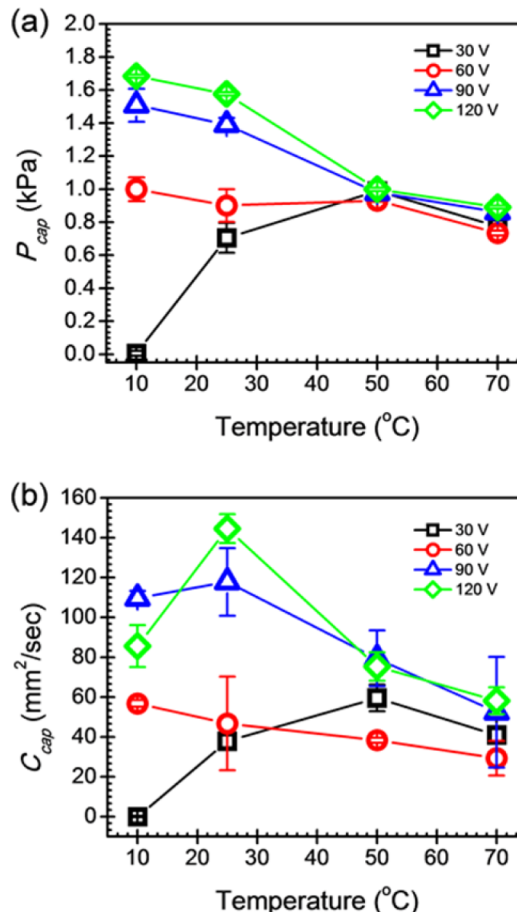


Figure 5. Changes in capillary pressure (a) and spreading speed constant (b) with respect to electric potential and electrolyte temperature during BDA. Four different electric potentials (30, 60, 90, and 120 V) and four different electrolyte temperatures (10, 25, 50, and 75 °C) were used to obtain the surfaces. The error bars indicate ± 1 standard deviation resulting from four measurements.

achieve the maximum capillary pressure was not always consistent with the value to obtain the maximum spreading speed. This highlights why both the capillary pressure and the spreading speed are necessary to evaluate and optimize superhydrophilic surfaces. For electrolyte temperatures less than 50 °C, the capillary pressure and the spreading speed constant increased with increasing electric potential. However, all surfaces showed similar capillary pressure and spreading speed at electrolyte temperatures greater than 50 °C (Figure 5). This behavior can be explained from the mechanisms of breakdown initiation and oxide layer dissolution. The electric potential to initiate breakdown is inversely proportional to the electrolyte temperature, as shown in eq 17. Therefore, high electrolyte temperatures are favorable for BDA at low electric potential. In contrast, because the dissolution rate of the oxide layer is proportional to the electrolyte temperature as shown in eq 18, low electrolyte temperatures promote thick and rough surfaces at high electric potential. At electrolyte temperatures exceeding 50 °C, both capillary pressure and spreading speed constant decrease due to significant dissolution of the oxide film into the electrolyte.

This theory is supported by SEM images of the surfaces at different electrolyte temperatures. The surfaces produced at an electrolyte temperature of 10 °C and electric potential of 30 V do not have porous structures, as shown in Figure 6a. Instead,

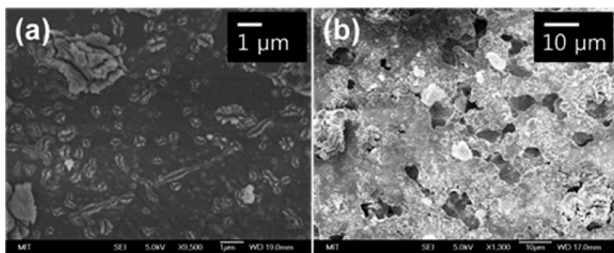


Figure 6. Sample SEM images of surfaces produced by BDA. At low electrolyte temperature and low electric potential (a), initiation of BDA is not facile; therefore, partially burst structures are observed on the surface produced at 30 V and 10 °C. When the electrolyte temperature was maintained at 75 °C during BDA, the highly interconnected porous structures shown in Figure 3a–c dissolve in the electrolyte, leaving smooth surfaces with large pores (b).

they feature small cracks that could not develop into pores. This suggests that high electric potentials are necessary to initiate BDA at low electrolyte temperatures. Conversely, the surfaces produced at high electrolyte temperatures show large porous structures, as shown in Figure 6b. This SEM image further suggests that dissolution at high electrolyte temperatures facilitates pore formation. The final weight of each substrate after BDA is further evidence of the influence of dissolution. When the electrolyte temperatures were lower than 50 °C, the weight of the substrate increased due to oxidation. However, for temperatures exceeding 50 °C, the substrate weight decreased due to the influence of dissolution. The relative amount of dissolution can be qualitatively measured by the amount of sediment in the electrolyte after the BDA processes. The sediments result from oxidized titanium through the dissolution process (eq 11) and are the same color as the porous oxide titanium structures shown in Figure 3a–c. As the electrolyte temperature increases, more sediment is observed.

To understand the role of nanoporous structures on capillary transport, TiO₂ nanoparticles were deposited on both bare titanium substrates and microporous surfaces by EPD. The capillary pressure and spreading speed were significantly affected by the deposition time (Figure 7). On the bare titanium substrate, the capillary pressure was linearly proportional to the deposition time, while the spreading speed decreased for deposition times longer than 90 s. To explain this result, the porosities were obtained from the deposition weights and the deposition heights. The porosity of the EPD surface can be estimated by

$$\text{Porosity} = 1 - \frac{\text{deposition weight}}{\text{deposition volume} \times \text{TiO}_2 \text{ density}} \quad (19)$$

The density of TiO₂ nanoparticles is 3.9 g/cm³ (Sigma-Aldrich, titanium oxide, anatase, nanopowder, <25 nm particle size, ≥99.7% purity). The deposition weight increases with EPD time, as shown in Figure 7c (red circles). The deposition volumes were calculated with the average deposition heights measured using a profilometer (measurement system: Tencor P-16 Surface Profilometer). The average deposition height increases with the EPD time (black boxes in Figure 7c). The

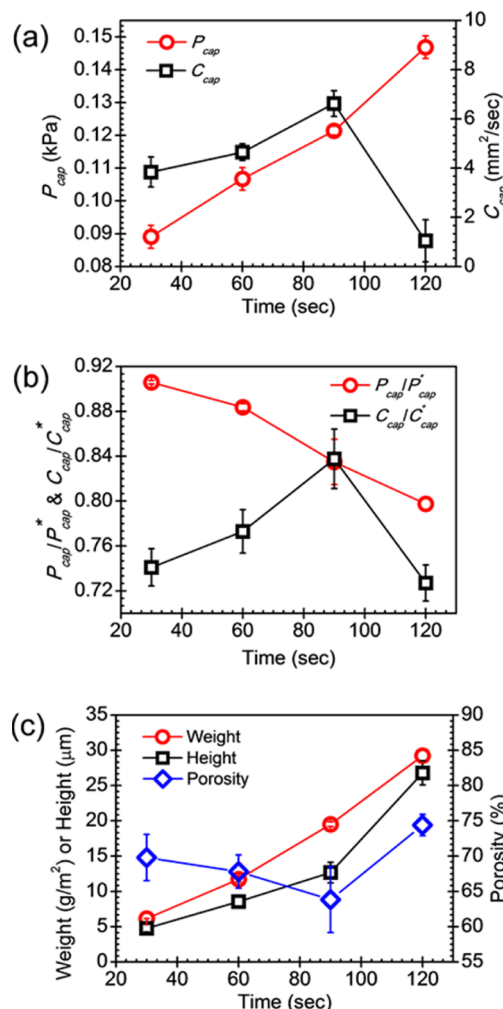


Figure 7. Capillary rise measurements of surfaces modified by EPD. EPD processes was conducted on bare titanium substrates (a) and on surfaces augmented by BDA (b). $P_{\text{cap}}/P'_{\text{cap}}$ and $C_{\text{cap}}/C'_{\text{cap}}$ are the ratios of capillary pressure and spreading speed constant before and after EPD, respectively. EPD was conducted at 30 V, and the BDA conditions were 120 V, 30 min, and 25 °C. The porosity of the deposits by EPD was calculated using the deposition weight per unit area and the deposition height (c). The error bars indicate ± 1 standard deviation resulting from three measurements.

porosity calculated by eq 19 shows a minimum at a deposition time of 90 s (blue diamonds in Figure 7c). It is clear that the spreading speed constant is inversely proportional to the porosity and the capillary pressure is proportional to the deposition height. A similar result, namely, increasing spreading speed with deposition thickness, was also observed in Cebeci et al.¹

For EPD on microporous surfaces produced by BDA, the capillary pressure shows opposite tendency as the bare substrate, decreasing with increasing deposition time. The spreading speed constant behaves similarly to the case of EPD on flat substrates. The nanoporous structures produced by EPD increase the viscous drag resistance; thus, the spreading speed constant displays a maximum irrespective of the initial substrate condition. However, microporous surfaces with thicker nanoporous layers (longer deposition time) show lower capillary pressures because the capillary pressure is affected by the additional viscous drag through the nanoporous structures.

The material compositions and atomic structures of the surfaces were investigated with X-ray diffraction (XRD) (Figure 8). The XRD patterns of a bare titanium substrate and TiO_2

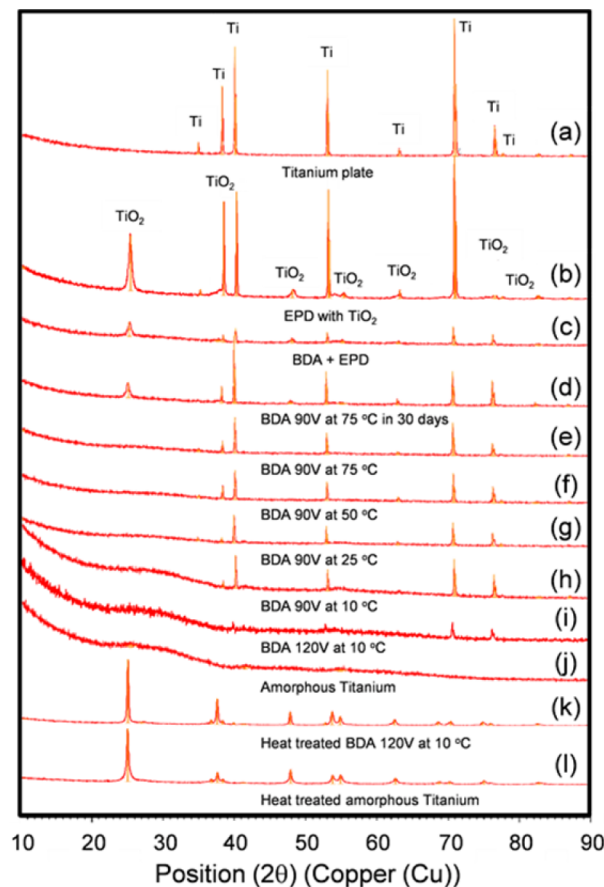


Figure 8. XRD patterns of the surfaces produced by EPD, BDA, and the hybrid BDA/EPD method. A bare titanium plate and the TiO_2 deposit surface were used as control XRD substrates, showing the spectra of titanium (a) and titanium dioxide (b). Surfaces produced by variations of EPD and BDA show aspects of both Ti and TiO_2 spectra. Sediments obtained after BDA show very weak peaks (j), which are indicative of amorphous titanium oxide.^{37,38} After heat treatment, the surface used in (i) and the sediments used in (j) show the spectra of anatase TiO_2 as shown in (k) and (l).

deposits were measured (Figure 8a and b) to serve as reference surfaces. Notably, the surface produced by the hybrid BDA/EPD method shows a combination of titanium and TiO_2 patterns (Figure 8c). Further, the amount of oxidized titanium produced by BDA affects the intensity of the peaks shown in Figure 8e–i. It is interesting to note that the surface produced at 120 V and 10 °C shows nearly no peak (Figure 8i), identical to the spectra of the sediment obtained after BDA (Figure 8j). According to other studies, the sediment can be assumed to be amorphous titanium oxide which lacks crystal structure.^{37,38} To confirm this hypothesis, we heat-treated the BDA surfaces and the sedimentation at 450 °C for 2 h to initiate crystallization. After heat treatment, the spectra of both samples (Figure 8k and l) are similar to anatase TiO_2 (Figure 8b). This result reveals that the porous structures created by BDA are composed of amorphous titanium oxide.

At electrolyte temperatures higher than 50 °C, oxidized titanium quickly dissolves into the electrolyte through the

reactions in eq 11. As a result, titanium peak patterns are observed on these surfaces, as shown in Figure 8e and f. It is worth noting that the BDA surfaces produced with high electrolyte temperature show different spectra after prolonged exposure to air (Figure 8d). This indicates that the surface titanium slowly oxidizes to titanium oxide. In addition, we found that the wettability is degraded by these transitions. EPD of high surface energy nanoparticles such as TiO_2 and SiO_2 alleviates the effect of surface oxidation in air. We believe that the nanoporous TiO_2 structures contribute to the higher durability of the BDA/EPD surfaces relative to the BDA surfaces. As explained in Cebeci et al.¹ and Drelich et al.,⁷ superhydrophilic surfaces can be achieved even with materials that have native contact angles higher than 65–70° if the surface roughness is extremely high. The nanoporous TiO_2 structures on the BDA surfaces greatly enhance the surface roughness. Therefore, the nano/microporous structures can maintain their superhydrophilicity longer than the BDA surfaces alone. In addition, we hypothesize that the enhanced durability is due to reduced oxidation of Ti relative to the BDA fabricated structures. To investigate this, we compared XRD data of the BDA/EPD and EPD surfaces immediately after they were produced and again 30 days later. The XRD patterns of the EPD surface did not change after 30 days. This suggests that the chemical composition and atomic structure of TiO_2 nanoparticles are relatively fixed. Therefore, the change in wetting properties of the BDA/EPD surface originated from property changes of the BDA surface underneath the EPD layer. Since the BDA/EPD surface shows higher durability than the BDA surface, we believe that the EPD layer on the BDA surface helped to retard the degradation of wetting properties.

We compare the degradation rates of five superhydrophilic surfaces that were produced by BDA with 120 V electric potential at 10, 25, 50, and 75 °C electrolyte temperature. We also examined the BDA/EPD method with BDA at 120 V and 10 °C and EPD at 30 V for 90 s. The five samples were maintained in laboratory air under ambient conditions for 30 days. The degradation rates were calculated by

$$\text{Degradation rate} = 1 - \frac{P_{\text{cap},2}}{P_{\text{cap},1}}$$

where $P_{\text{cap},1}$ and $P_{\text{cap},2}$ are the initial and final capillary pressures, respectively, of the surface. Table 1 shows the degradation rates

Table 1. Changes in Capillary Pressure for Five Superhydrophilic Surfaces 30 Days after Fabrication

	BDA					BDA/EPD
	10 °C	25 °C	50 °C	75 °C		
degradation rate	23%	17%	21%	21%	7%	

of the prepared surfaces. The BDA surfaces produced with different electrolyte temperatures show similar degradation rates, and the average degradation rate is 20%. As expected, the lowest degradation rate was observed from the BDA/EPD surface due to the nanoporous structures, as mentioned above.

From eqs 2 and 3, we know that the pore size strongly influences capillary pressure and spreading speed constant. To determine the role of electric potential in BDA, surface roughness was measured using the profilometer. Surface roughness was measured for the substrates used in Figure 5 with the exception of the 50 and 75 °C electrolytes. At these

high electrolyte temperatures, BDA resulted in highly interconnected pores, as shown in Figure 6b; therefore, it is not appropriate to compare with other surfaces. To show the correlations between the wetting properties of the BDA surfaces and the surface structure, first we compare the effective pore radius with the surface roughness, as shown in Figure 9a. The effective pore radius can be considered a key

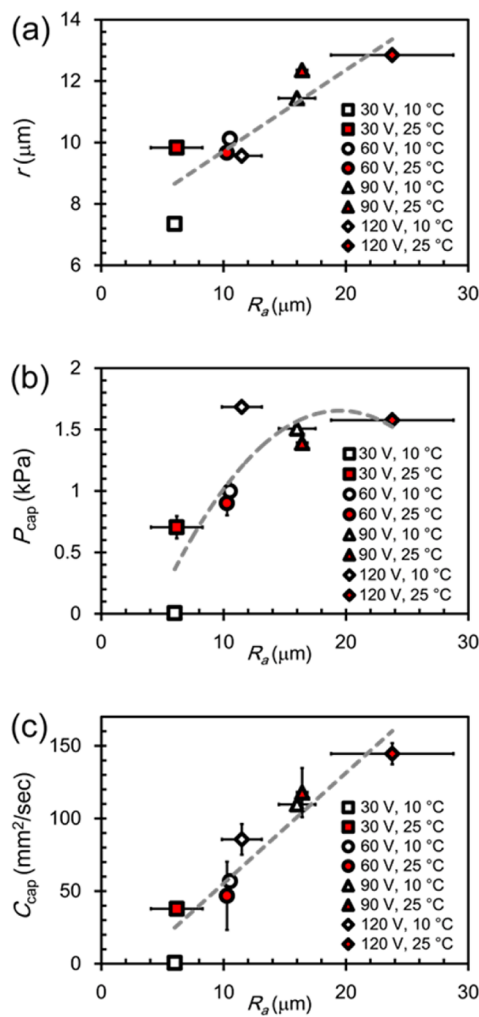


Figure 9. Plots of the pore radius (a), the capillary pressure (P_{cap}) (b), and the spreading speed constant (C_{cap}) (c) with respect to surface roughness. The pore radius obtained by eq 4 with P_{cap} and C_{cap} shown in parts b and c is linearly proportional to the surface roughness (a). The box, circle, triangle, and diamond symbols indicate the electric potentials of 30, 60, 90, and 120 V, respectively, used in the BDA processes. The fill colors indicate the electrolyte temperature, 10 °C (white) and 25 °C (red). Morphological data was obtained with a profilometer (measurement system: Tencor P-16 Surface Profilometer). The error bars indicate ± 1 standard deviation resulting from four measurements.

parameter to characterize the surface structure. The pore radius can be calculated by eq 4 with the values of P_{cap} and C_{cap} obtained from capillary rise measurements (CRM). In Figure 9a, we confirm that the pore radius is roughly linearly proportional to the surface roughness. Capillary pressure asymptotes with surface roughness (and therefore pore radius), as shown in Figure 9b. However, the spreading speed constant is linear with surface roughness and pore radius (Figure 9c). This result reveals that capillary pressure and spreading speed

can be tuned with both electric potential and electrolyte temperature because the surface roughness and pore radii are changed.

From the relation between electric potentials and spreading speed constants (Figure 9), we developed superhydrophilic surfaces that have unconventional capillary flows. To vary the electric potentials continuously through an electrode used in BDA, various profiles of electrodes were used, as shown in Figure 10 from case 1 to case 3. In addition, triangle substrates

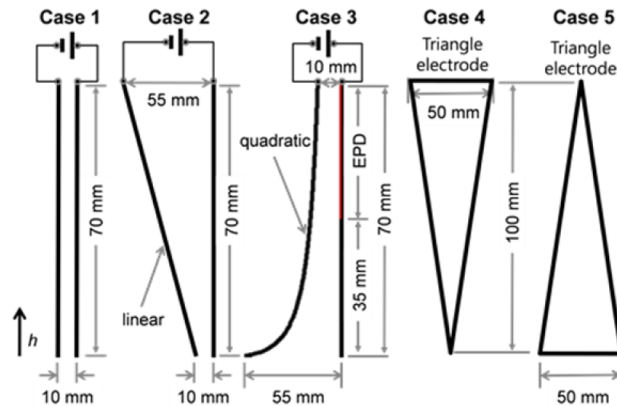


Figure 10. Schematic illustrations of electrode gap profiles and electrode shapes used to demonstrate capillary transport modification with BDA and EPD. Case 1 was used as a reference with a constant gap distance (10 mm) and a rectangular electrode shape (10 mm \times 70 mm). In cases 2 and 3, the electric potentials vary with gap distance between anode and cathode electrodes, with identical electrode cross-sectional area as case 1. In case 3, TiO_2 nanoparticles were partially deposited on the surface produced by BDA using EPD. In cases 4 and 5, triangular electrodes were used with the same electrode gap distance as case 1 (10 mm).

were used to demonstrate unconventional flows can be achieved with different shapes of electrodes (cases 4 and 5 in Figure 10). The same size (10 mm \times 70 mm) of rectangular electrodes was used in cases 1–3. Constant electrode gap distance (10 mm) was used in cases 1, 4, and 5. To show the effect of nanoporous layers on capillary flows, TiO_2 nanoparticles were partially deposited by EPD with constant electric potential (30 V) for 5 min on the surface produced by BDA with the electrode profile given in case 3.

With the electrodes designed in Figure 10, various unconventional capillary flows were obtained (Figure 11). The results of CRM show superhydrophilic surfaces where the square of capillary height can be nonlinear in time. Case 2 shows faster spreading speeds than case 1 for short times but becomes slower over time. We attribute this result to pore radius changes resulting from the varying electrode gap distance. Notably in case 3, the surface with partial TiO_2 deposit via EPD, there is a discontinuous change of spreading speed. This shows that the nanoporous structures produced by EPD can locally change the spreading speed. Cases 4 and 5 show that capillary flows can depend on the electrode shapes and orientation. For case 4, the spreading speed constant increases with time, while case 5 is nearly identical to case 1. The trend lines in Figure 11 are linear and quadratic fitting lines of the experimental data. However, theoretical predictions for the capillary flows are possible but beyond the scope of this paper. We are now preparing a follow-up paper investigating the effects of electrode configurations and shapes on capillary

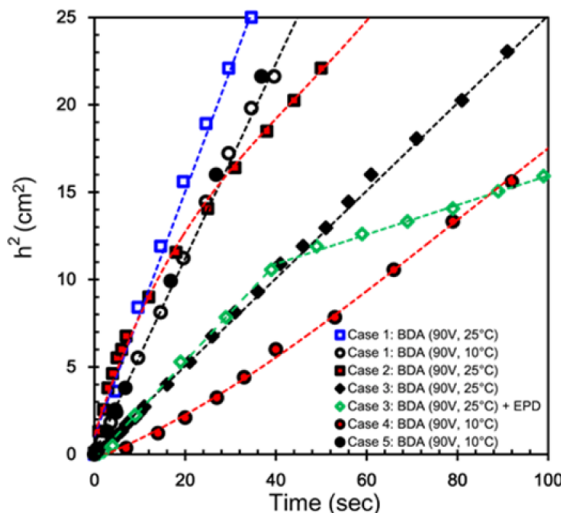


Figure 11. Square of measured capillary rise height with respect to time for superhydrophilic surfaces produced by the BDA and EPD methods presented in Figure 10. In the BDA processes, two different electrolyte temperatures (10 and $25\text{ }^\circ\text{C}$) and one electric potential (90 V) were used. In the EPD process, 30 V was supplied for 5 min to deposit TiO_2 nanoparticles. In cases 2–4, the square of capillary height is nonlinear in time, unlike conventional capillary flows. With augmentation via EPD, the spreading speed can be discontinuously changed, as shown in case 3.

flows. The approach to predict the capillary flows is as follows. The capillary pressure and the spreading speed constant are functions of the rise height (h shown in Figure 10) depending on the configuration and shape of the electrode in the BDA method. As a result, we can formulate the general capillary flow equations in terms of the capillary pressure and spreading speed constant.

CONCLUSIONS

Superhydrophilic surfaces with hierarchical micro- and nanoscale pores were produced via a hybrid BDA/EPD method. BDA effectively creates microscale porous structures on titanium substrates. BDA morphology is a function of electric potential and electrolyte temperature in constant pH electrolytes. We found that there were optimal values of electric potential and electrolyte temperature to obtain high capillary pressure and spreading speed. The electrolyte temperature affects both the breakdown potential and the thickness of the resulting oxide layer. High electrolyte temperatures decrease the breakdown potential but also decrease the oxide layer thickness due to dissolution. These opposing contributions result in an optimal electrolyte temperature for a given electric potential. Amorphous titanium oxide layers provide high surface energy to the microporous structures, resulting in highly wetting surfaces.

Nanoporous titanium dioxide layers were deposited on the microporous structures produced by BDA using EPD. With the EPD process, capillary pressure and spreading speed were precisely controlled by the deposited mass. The nanoporous films offer stability to the BDA surfaces. The surfaces produced by the hybrid method showed significantly higher capillary pressure and spreading speed than the surfaces produced by EPD alone. Ultimately, the characteristics of the superhydrophilic surfaces are mainly controlled by BDA, but the

EPD films can offer various surface energies and nanostructures to microporous surfaces produced by BDA.

We have also presented various methods to achieve unconventional capillary flows. These capillary flows showed varying spreading speed constants at different locations on the substrate. The methods presented can be used to create low-cost superhydrophilic surfaces with specially tailored transport properties. Furthermore, the hybrid BDA/EPD method has great potential to be used for various applications requiring high surface area or a large number of reacting sites. Numerous material compositions and nanostructures can be effectively altered by EPD with different kinds of nanoparticles, depending upon the desired application.

AUTHOR INFORMATION

Corresponding Author

*Phone: 617-253-9379. E-mail: crb@mit.edu.

Notes

The authors declare no competing financial interest.

ACKNOWLEDGMENTS

The authors are grateful to Mr. Dongkyu Lee for help with the XRD system. This work made use of the MRSEC Shared Experimental Facilities at MIT, supported by the National Science Foundation under award number DMR-08-19762. Funding was provided by Battelle Memorial Institute.

REFERENCES

- Cebeci, F. Ç.; Wu, Z.; Zhai, L.; Cohen, R. E.; Rubner, M. F. *Langmuir* **2006**, *22*, 2856–2862.
- Watanabe, T.; Nakajima, A.; Wang, R.; Minabe, M.; Koizumi, S.; Fujishima, A.; Hashimoto, K. *Thin Solid Films* **1999**, *351*, 260–263.
- Chen, Y.; Mo, D.; Zhao, H.; Ding, N.; Lu, S. *Sci. China, Ser. E: Technol. Sci.* **2009**, *52*, 1596–1600.
- Youngsuk, N.; Sharratt, S.; Byon, C.; Sung Jin, K.; Ju, Y. S. *J. Microelectromech. Syst.* **2010**, *19*, 581–588.
- Takata, Y.; Hidaka, S.; Cao, J. M.; Nakamura, T.; Yamamoto, H.; Masuda, M.; Ito, T. *Energy*, **30**, 209–220.
- Feng, X. J.; Jiang, L. *Adv. Mater.* **2006**, *18*, 3063–3078.
- Drellich, J.; Chibowski, E.; Meng, D. D.; Terpilowski, K. *Soft Matter* **2011**, *7*, 9804–9828.
- Wenzel, R. N. *Ind. Eng. Chem.* **1936**, *28*, 988–994.
- Yu, J.; Zhao, X.; Zhao, Q.; Wang, G. *Mater. Chem. Phys.* **2001**, *68*, 253–259.
- Shi, F.; Chen, X. X.; Wang, L. Y.; Niu, J.; Yu, J. H.; Wang, Z. Q.; Zhang, X. *Chem. Mater.* **2005**, *17*, 6177–6180.
- Kakade, B.; Mehta, R.; Durge, A.; Kulkarni, S.; Pillai, V. *Nano Lett.* **2008**, *8*, 2693–2696.
- Lai, Y.; Chen, Y.; Tang, Y.; Gong, D.; Chen, Z.; Lin, C. *Electrochim. Commun.* **2009**, *11*, 2268–2271.
- McDonald, B. T.; Cui, T. *J. Colloid Interface Sci.* **2011**, *354*, 1–6.
- Yu, X.; Wang, Z. Q.; Jiang, Y. G.; Zhang, X. *Langmuir* **2006**, *22*, 4483–4486.
- Siebold, A.; Walliser, A.; Nardin, M.; Oppliger, M.; Schultz, J. *J. Colloid Interface Sci.* **1997**, *186*, 60–70.
- Washburn, E. W. *Phys. Rev.* **1921**, *17*, 273.
- Joung, Y. S.; Buie, C. R. *Langmuir* **2011**, *27*, 4156–4163.
- Lai, Y. K.; Chen, Y. C.; Tang, Y. X.; Gong, D. G.; Chen, Z.; Lin, C. *J. Electrochem. Commun.* **2009**, *11*, 2268–2271.
- Ohtsuka, T.; Masuda, M.; Sato, N. *J. Electrochem. Soc.* **1985**, *132*, 787–792.
- Vermilyea, D. A. *J. Electrochem. Soc.* **1955**, *102*, 207–214.
- Yahalom, J.; Zahavi, J. *Electrochim. Acta* **1970**, *15*, 1429–1435.
- Zhao, J.; Wang, X.; Chen, R.; Li, L. *Solid State Commun.* **2005**, *134*, 705–710.

- (23) Macák, J. M.; Tsuchiya, H.; Schmuki, P. *Angew. Chem., Int. Ed.* **2005**, *44*, 2100–2102.
- (24) Sun, L.; Zhang, S.; Sun, X. W.; Wang, X.; Cai, Y. *Langmuir* **2010**, *26*, 18424–18429.
- (25) Gong, D.; Grimes, C. A.; Varghese, O. K.; Hu, W.; Singh, R. S.; Chen, Z.; Dickey, E. C. *J. Mater. Res.* **2001**, *16*, 3331–3334.
- (26) Ghicov, A.; Tsuchiya, H.; Macak, J. M.; Schmuki, P. *Electrochim. Commun.* **2005**, *7*, 505–509.
- (27) Cai, Q.; Paulose, M.; Varghese, O. K.; Grimes, C. A. *J. Mater. Res.* **2005**, *20*, 230–236.
- (28) Kaneko, S.; Chen, Y.; Westerhoff, P.; Crittenden, J. C. *Scr. Mater.* **2007**, *56*, 373–376.
- (29) Henry, D. C. *Proc. R. Soc. London, Ser. A* **1931**, *133*, 106–129.
- (30) Muñoz-Portero, M. J.; García-Antón, J.; Guiñón, J. L.; Leiva-García, R. *Corros. Sci.* **2011**, *53*, 1440–1450.
- (31) Sato, N. *Electrochim. Acta* **1971**, *16*, 1683–1692.
- (32) Mazhar, A. A. *J. Appl. Electrochem.* **1990**, *20*, 494–499.
- (33) Blackwood, D. J.; Peter, L. M.; Williams, D. E. *Electrochim. Acta* **1988**, *33*, 1143–1149.
- (34) Breiter, M. W. *Electrochim. Acta* **1970**, *15*, 1195–1200.
- (35) Bockris, J. O. M.; Potter, E. C. *J. Chem. Phys.* **1952**, *20*, 614–628.
- (36) Vermilyea, D. A. *J. Electrochem. Soc.* **1957**, *104*, 542–546.
- (37) Hart, J.; Bourgeois, L.; Cervini, R.; Cheng, Y. B.; Simon, G.; Spiccia, L. *J. Sol-Gel Sci. Technol.* **2007**, *42*, 107–117.
- (38) Yin, L.; Gwak, Y.; Yu, C. *J. Mater. Sci.* **2011**, *46*, 6835–6840.